Supplementary Material of the Research Report:

" Platonic and Archimedean geometries in multi-component elastic membranes "

Authors:

Graziano Vernizzi[1♯], Rastko Sknepnek[1], Monica Olvera de la Cruz[1,2,3,*]

[1]Department of Materials Science and Engineering, Northwestern University, Evanston, IL 60208, USA.

[2]Department of Chemical & Biological Engineering, Northwestern University, Evanston, IL 60208, USA.

[3]Department of Chemistry, Northwestern University, Evanston, IL 60208, USA.

[*]To whom correspondence should be addressed. E-mail: m-olvera@northwestern.edu

[♯] Present address: Department of Physics & Astronomy, Siena College, Loudonville, NY 12211, USA.

Materials and Methods.

1. Continuum elastic theory for a disclination on a heterogeneous two-component membrane

In order to gain a better insight into the elastic behavior of a two-component membrane, we analyze in the following section the simpler problem of determining the elastic energy

of a single disclination on a disk, made of two elastic components and in the case of flat geometry.

Flat disk

The stretching energy of a flat isotropic thin plate parallel to the plane $z = \{x, y\}$ is traditionally written as (1):

$$F_s = \int d^2 z\, \mu\, Tr(U^2) + \frac{\lambda}{2} Tr(U)^2 ,$$

where λ and μ are the two-dimensional Lamé coefficients, and U is the two-dimensional strain tensor $U \equiv u_{ij} = (\partial_i u_j + \partial_j u_i)/2$ at small displacements u_i from the equilibrium configuration. The equilibrium equations are $\partial_i \sigma_{ij} = 0$, where $\Sigma \equiv \sigma_{ij} = 2\mu U + \lambda Tr(U)I$ is the stress tensor. The strain tensor can be obtained by inverting the stress-strain equation: $U = \frac{1+v}{Y}\Sigma - \frac{v}{Y} Tr(\Sigma)I$, where Y and v are the two-dimensional Young's modulus and Poisson ratio. They are both functions of the two-dimensional Lamé coefficients:

$$\begin{cases} Y = \dfrac{4\mu(\mu + \lambda)}{2\mu + \lambda} \\ v = \dfrac{\lambda}{2\mu + \lambda} \end{cases} .$$

All the equations above are local in character, and therefore they hold also in the inhomogeneous case where the elastic coefficients depend on the position $Y = Y(\vec{r}), v = v(\vec{r})$. For two-dimensional geometries, it is customary to introduce the

Airy stress function χ, which in polar coordinates $\{x = r\cos\theta, y = r\sin\theta\}$ relates to the stress tensor simply by:

$$\sigma_{rr} = \partial_r\chi / r + \partial_{\theta\theta}^2\chi / r^2$$
$$\sigma_{\theta\theta} = \partial_{rr}^2\chi$$
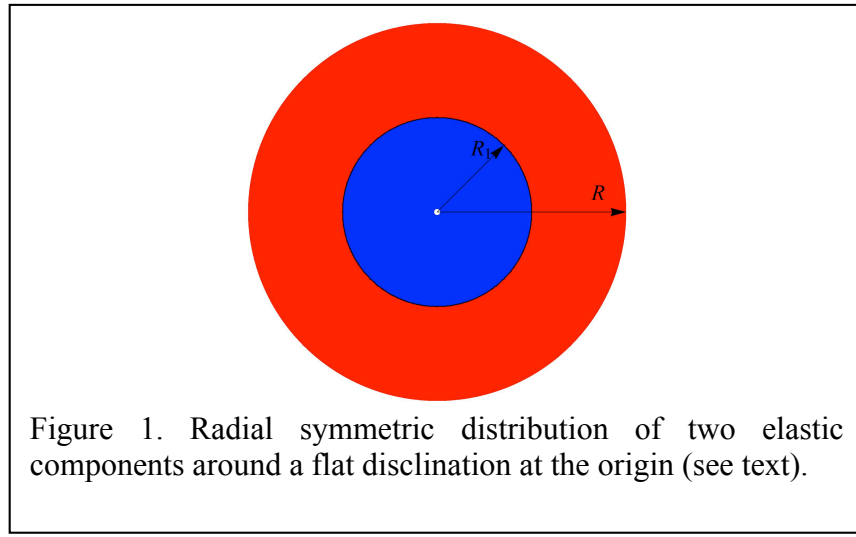$$\sigma_{r\theta} = -\partial_r(\partial_\theta\chi / r)$$

While *any* function χ yields a stress tensor that identically satisfies the equilibrium equations $\partial_i\sigma_{ij} = 0$, not all functions χ correspond to a unique field of displacement vectors u_i. The so-called compatibility equation that guarantees a unique solution of the equilibrium equations in terms of displacement vectors u_i is a well-known biharmonic equation. In the case of constant Y and v and a flat disclination at the origin $r=0$, it reads (*2*):

$$\nabla^4\chi = \nabla^2(\nabla^2\chi) = s\,Y\delta(\vec{r}),$$

where $\nabla^2 = r^{-1}\partial_r r\partial_r + r^{-2}\partial_\theta^2$ is the Laplacian in polar coordinates, $\delta(\vec{r})$ is the two-dimensional Dirac delta function, and s is the disclination charge. In this work, we are mostly interested in five-fold disclinations and therefore set $s=2\pi/6$.

When the Young's modulus and the Poisson ratio are not constant functions, the compatibility equation is considerably more complicated but nonetheless straightforward to obtain. In the particular case of complete radial symmetry, $\boxed{Y = Y(r), v = v(r)}$, we have:

$$\boxed{\frac{1}{r}\frac{\partial}{\partial r}\left(\frac{Y'(r)}{Y^2(r)}(v(r)\chi'(r) - r\chi''(r)) + \frac{r(\chi''(r) + r\chi'''(r)) - (1 + rv'(r))\chi'(r)}{rY(r)}\right) = s\delta(\vec{r})}$$

Figure 1. Radial symmetric distribution of two elastic components around a flat disclination at the origin (see text).

We solve this equation for the case of piecewise-constant radial distribution of two elastic components (see Figure 1). For simplicity, we assume that the two components having the same (constant) Poisson ratio $v_A = v_B = v$, but different Young's moduli Y_1, Y_2. The first component occupies a circular region with radius $r = R_1$, and the second component occupies the circular ring between $r = R_1$ and $r = R$.

The solution can thus be found by first determining the general integral in the two regions, $0 < r < R_1$ and $R_1 < r < R$, and then by imposing suitable boundary conditions that connect the two solutions. Away from the boundaries, where the Young's modulus is constant, we have $Y'(r) = 0$. And the equation obviously reads $\nabla^4 \chi = 0$, which has four independent solutions that do not depend on the polar angle:

$$\chi = A, \chi = \log(r), \chi = r^2, \chi = r^2 \log r.$$

Therefore, the general solution in the bulk regions is given by the (piecewise) linear combination:

$$\chi(r) = \begin{cases} A_1 + B_1 \log(r) + C_1 r^2 + D_1 r^2 \log(r), & r < R_1 \\ A_2 + B_2 \log(r) + C_2 r^2 + D_2 r^2 \log(r), & R_1 < r < R \end{cases}$$
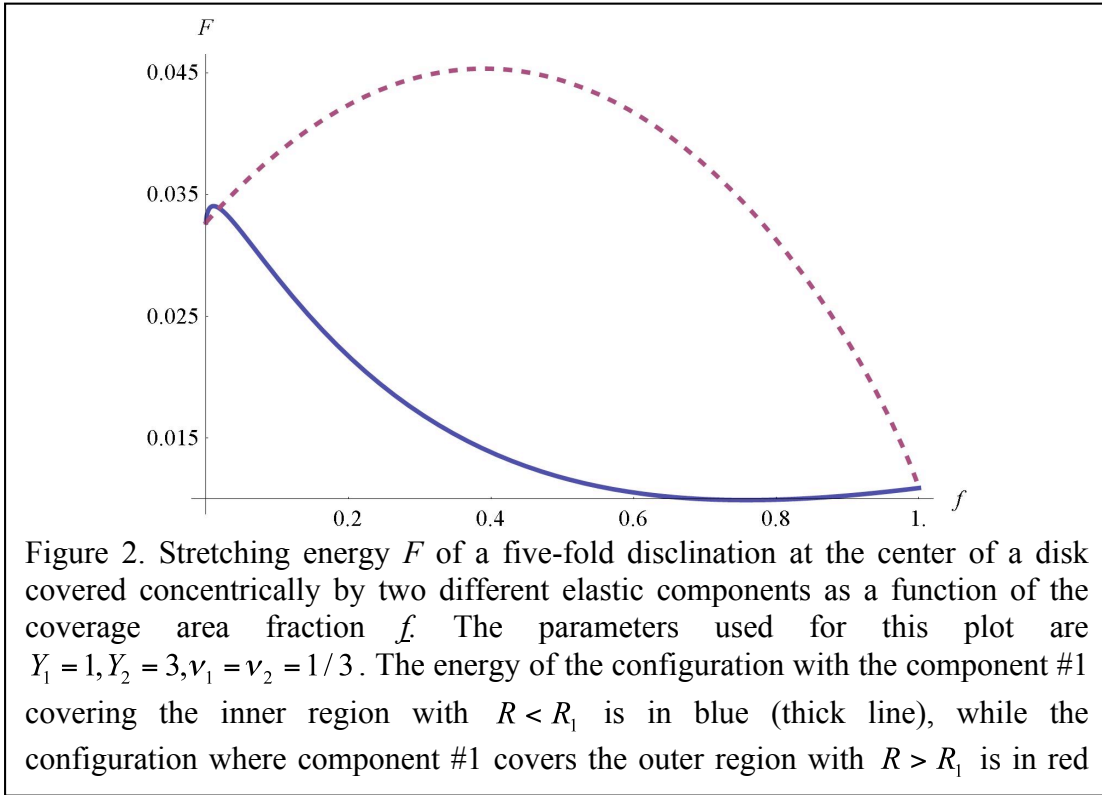
The coefficients A_i, B_i, C_i, D_i can be determined by imposing the following boundary conditions. First, the radial components of the stress tensor $\sigma_{r\theta} = 0$, $\sigma_{rr} = A_i + B_i / r^2 + 2D_i \log(r)$ should vanish at $r = R$, since the membrane is assumed to be unconstrained at the edge. Second, the Airy function χ and the stress tensor σ must be continuous across the boundary at $r = R_1$ in order to have equilibrium. Third, since the Airy function is defined up to an additive constant, we assume its value at the origin to be $\chi(0) = 0$. Moreover, the requirement that the displacement u_i must be finite at $r = 0$ implies $B_1 = 0$. Finally, by applying the Gauss theorem to the original differential equation over a disk of radius $r < R_1$ and $r > R_1$, we get $D_1 = sY_1 / 8\pi$ and $D_2 = sY_2 / 8\pi$. We obtain:

$$\chi(r) = \begin{cases} \dfrac{Y_1 R^2 s}{16\pi} \tilde{r}\left(\tilde{Y} - 2 + \tilde{R}_1^2(1-\tilde{Y}) + 2(\tilde{Y}-1)\log\tilde{R}_1 + 2\log\tilde{r}\right) & r < R_1 \\ \dfrac{Y_1 R^2 s}{16\pi}\left(-\tilde{Y}\tilde{r}^2 - (\tilde{Y}-1)\tilde{R}_1^2(\tilde{r}^2 - 2 + \log\tilde{R}_1^2) + 2(\tilde{Y}\tilde{r}^2 + (\tilde{Y}-1)\tilde{R}_1^2)\log\tilde{r}\right) & R_1 < r < R \end{cases}$$, whe

re we introduced the dimensionless parameters $\tilde{r} = r / R$, $\tilde{R}_1 = R_1 / R$ and $\tilde{Y} = Y_2 / Y_1$. From this expression we can compute the stress tensor and the strain tensor, from which the initial integral for the stretching energy follows as well. The result is lengthy but straightforward. It is useful to express R_1 in terms of the area fraction f occupied by the #1-component, that is f=area(#1)/(area(#1)+area(#2)), or equivalently, $R_1 = \sqrt{f}R$, and to let $F_{\#1<R_1}(f)$ be the stretching energy for such a configuration. We verified that for $Y_1 = Y_2$, we recover the classic result $F_{\#1<R_1}(f) = Y_1 R^2 s / 32\pi$ (2). Moreover, we are interested in comparing $F_{\#1<R_1}(f)$ with the stretching energy $F_{\#2<R_1}(f)$ for the case where

the #2-component occupies the inner region (and $R_1 = \sqrt{1-f}R$). The two energies are

plotted in Figure 2. Two features can be observed: first, the stretching energy scales as

$\sim R^2$ for large radii, as expected. Secondly, the less stiff component (i.e. having smaller

Young's modulus) tends to occupy the region over the disclination, except at very small

fraction values where the situation is the opposite.

Figure 2. Stretching energy F of a five-fold disclination at the center of a disk covered concentrically by two different elastic components as a function of the coverage area fraction f. The parameters used for this plot are $Y_1 = 1, Y_2 = 3, v_1 = v_2 = 1/3$. The energy of the configuration with the component #1 covering the inner region with $R < R_1$ is in blue (thick line), while the configuration where component #1 covers the outer region with $R > R_1$ is in red

We compared our analytic result with a numerical Monte Carlo simulation. Some

snapshots of the simulations are presented in Figure 3, and a plot of the corresponding

radial density of the two components and the stretching energy are shown in Figure 4 and

Figure 5, respectively. Figure 4 confirms the tendency for the weak component to occupy

the region close to the center; even though the contribution from the disk boundaries is not negligible (our simple theoretical analysis neglects the details of boundary effects). We note that the curve in Figure 5 has a trend in qualitative agreement with the exact curve in Figure 2. Finally, Figure 6 shows how the total stretching energy is distributed around the five-fold disclination. While most of the stretching energy is concentrated near the center of the disk, where the five-fold disclination is located and therefore rich in the soft component, there are important boundary effects. Such terms break the axial (rotational) symmetry, which we have assumed in our theoretical analysis and, in our opinion, are ultimately the consequence of the discreteness associated with the numerical model used in our Monte Carlo simulations.
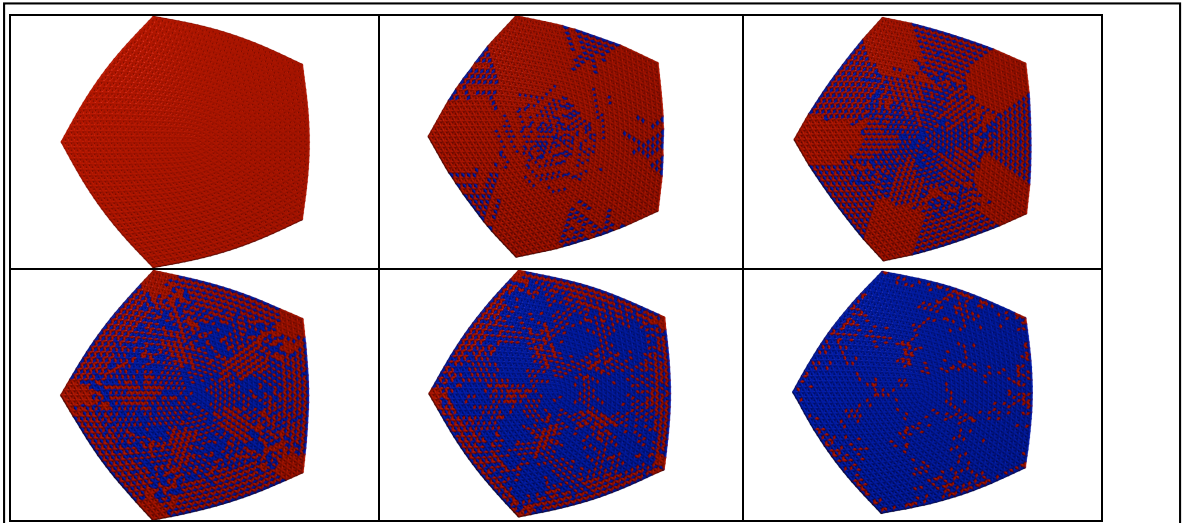

Figure 3. Snapshots of Monte Carlo configurations at different relative ratio of the two-components (from left to right, top to bottom, 0, 0.1, 0.3, 0.5, 0.7, and 0.9 , respectively) with a flat 5-fold disclination. The weak component (in blue) has Young modulus $Y = 11.5$ (in arbitrary units) while the strong component (in red) has $Y = 115$.
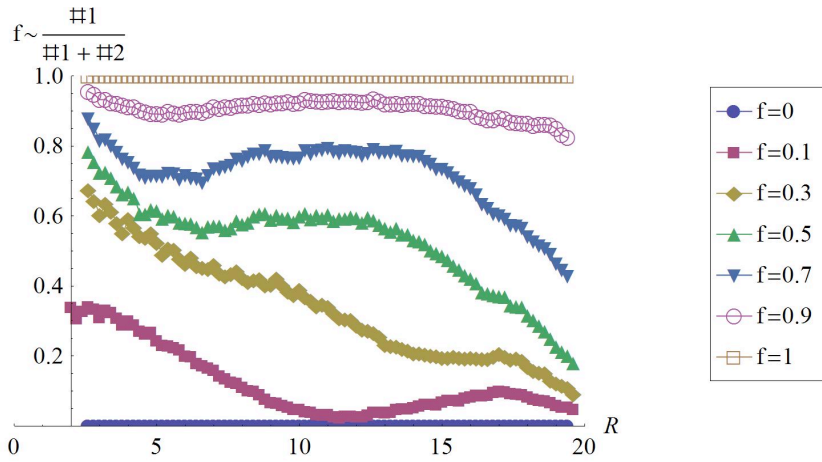
Figure 4. Relative density along radial direction of the two components at different ratios f, for the flat configurations in Figure 3. The inner region at small R is occupied mostly by the softer component.
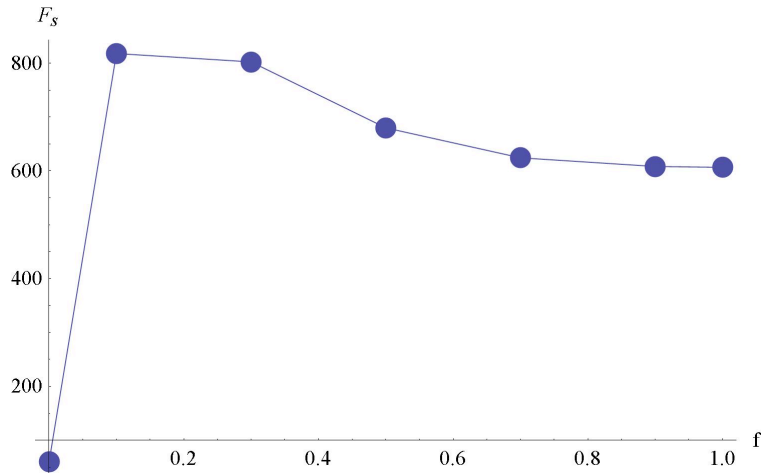

Figure 5. Total stretching energy F of the configurations presented in Figure 3, as a function of the relative fraction f. The dots (simulation data) are joined with lines just to help the eye.
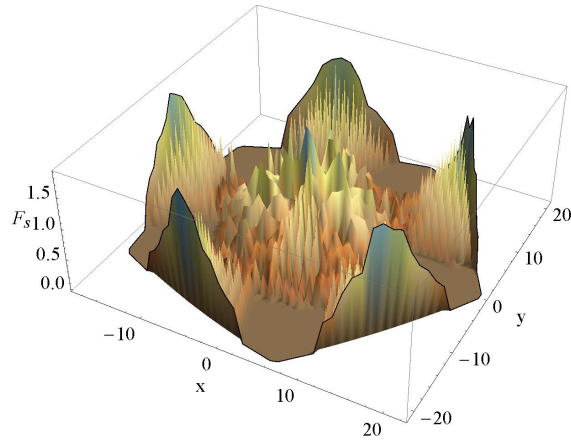
Figure 6. Three-dimensional plot of the stretching energy density at $f=0.3$, as a function of the position on the disk. Besides boundary effects, most of the stretching energy is condensed around the central five-fold disclination rich with the soft-component.

Out-of-plane bending of a disk

In Figure 7 we show snapshots of the buckled five-fold disclination for six different relative fractions of the elastic components. For discussion, see the Model and Method section in the article.

Finally, in Figure 8 we plot the bending energy of the configurations (similar to the ones in Figure 7) at different area fractions. We verified that the decay of the energy with the area fractions is logarithmic, as predicted in our theoretical analysis presented in the Model and Method section in the article.
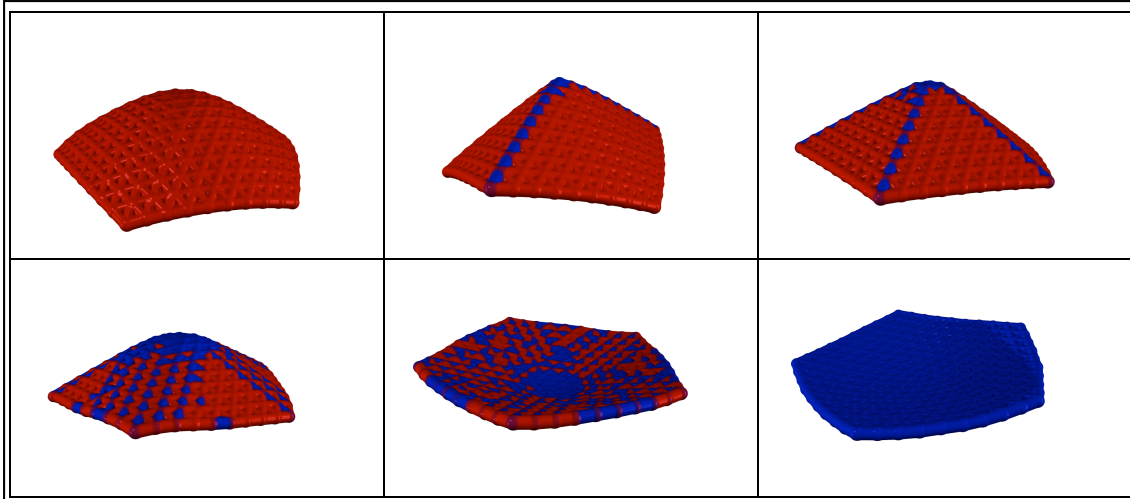
Figure 7. The buckling of a five-fold disclination at the center of a disk with radius R=10 (lattice units). From top to bottom, left to right, the relative fractions are: f=0, 0.1, 0.35, 0.5, 0.7, 1. The component in blue has elastic parameters $Y_A = 1.15$, $\kappa_A = 0.87$ and favors flat configurations while the component in red has $Y_B = 115$, $\kappa_B = 26$ which favors buckling. Note that slight curvature of the bottom right configuration is the low-wavelength thermal excitation of the plate and has nothing to do with the disclination induced buckling.
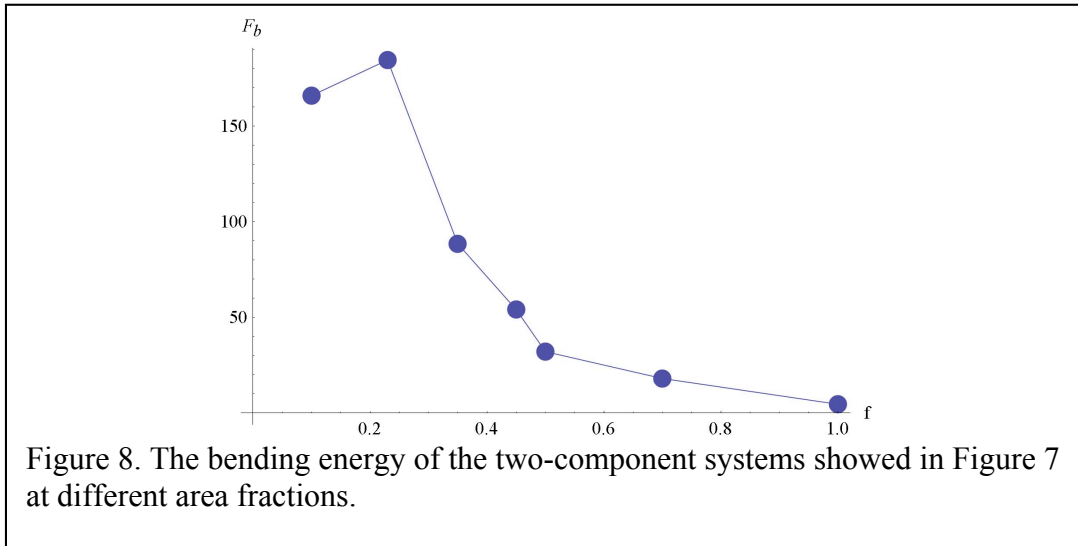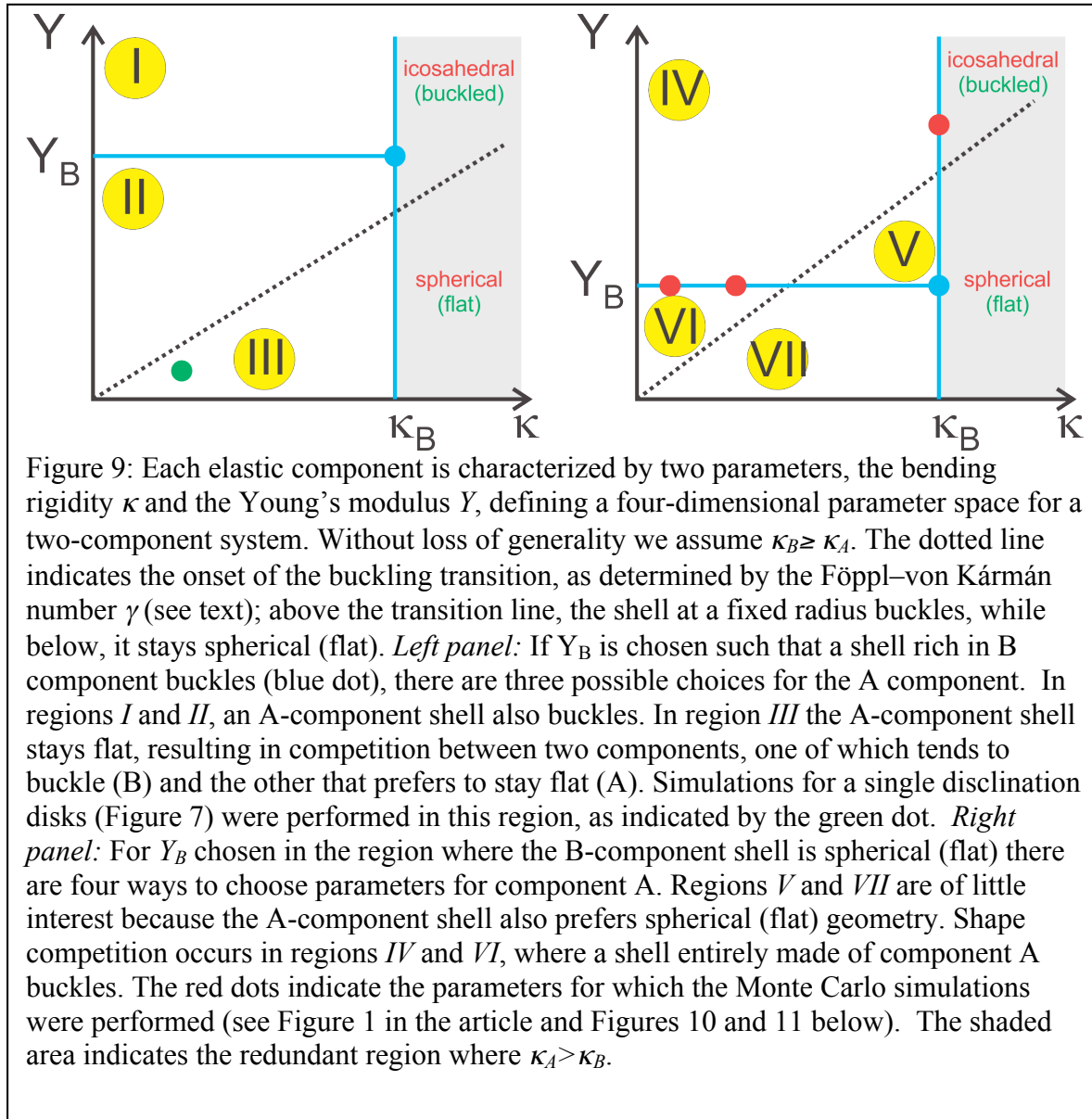

Figure 8. The bending energy of the two-component systems showed in Figure 7 at different area fractions.

Parameter space for a two-component system

In Figure 9 we show a cartoon of the parameter space and indicate regions where the shape competition between the two elastic components occurs (regions III, IV, and VI in Figure 9; for discussion see the caption). The onset of a buckling transition, controlled by the Föppl–von Kármán number $\gamma=YR^2/\kappa$, where R is the shell radius, is indicated by the dotted line. Note that, for fixed Y and κ, the slope of the transition line is inversely proportional to R^2, consistent with the observation that large homogeneous shells are predominantly icosahedral. In order to observe faceting in a shell with a given radius, at least one of the components would have to have a large bending rigidity while maintaining a low Young's modulus; that is, it would greatly prefer stretching over bending. On the other hand, for very small shells, the transition line approaches the Y-axis, and the material would have to have exceedingly high Young's modulus and a very low bending rigidity. Further, for small shells, the discrete (atomistic) nature of the material plays an important role, and our analysis based on the continuum elastic theory becomes questionable. Therefore, in both cases, for the shape competition to take place, at least one component should have either an relatively large or relatively low Y-to-κ ratio. In summary, faceting effects reported in this study are expected to occur for a narrow range of shell sizes, where the shape competition is consistent with the elastic parameters of soft materials.
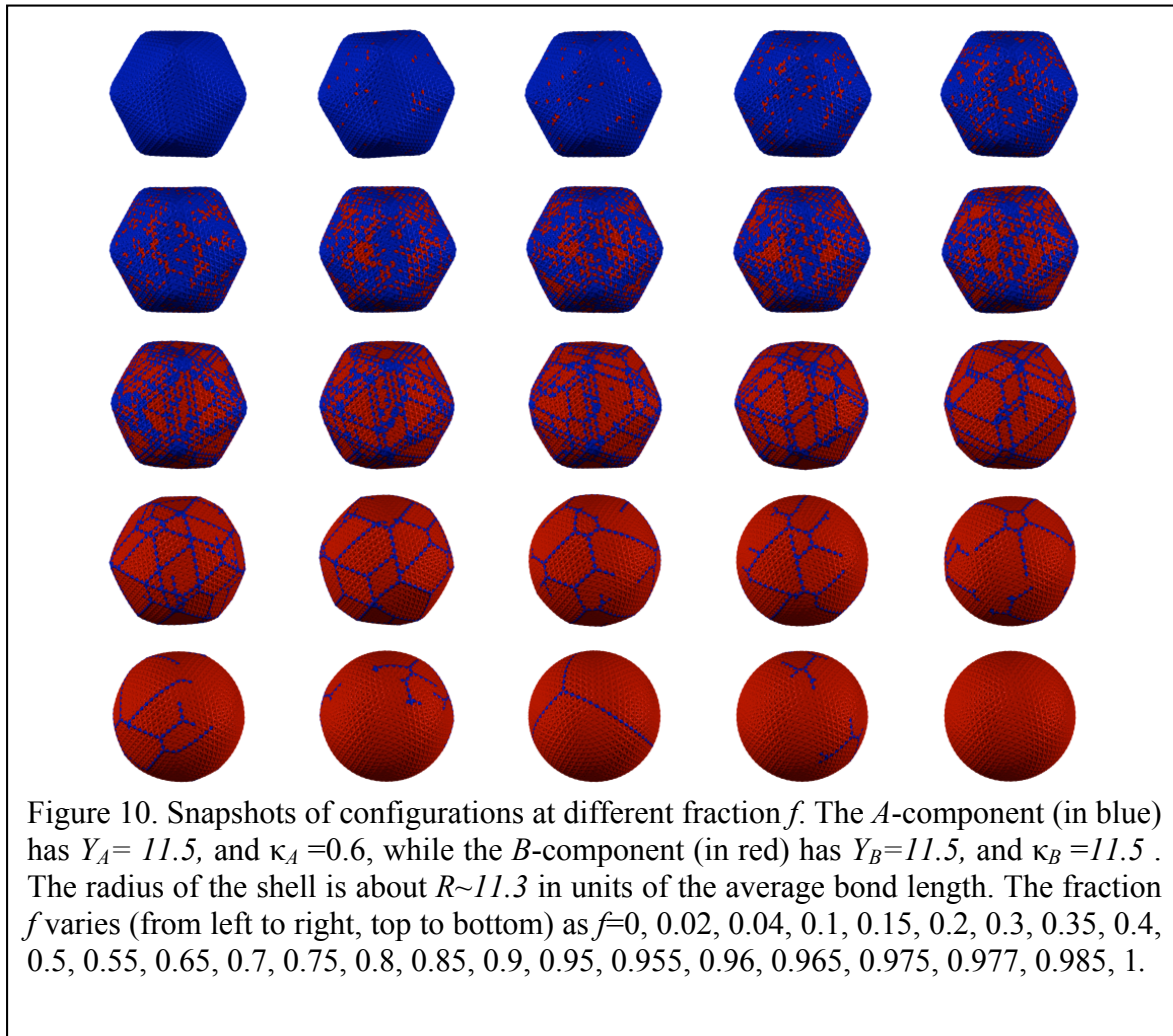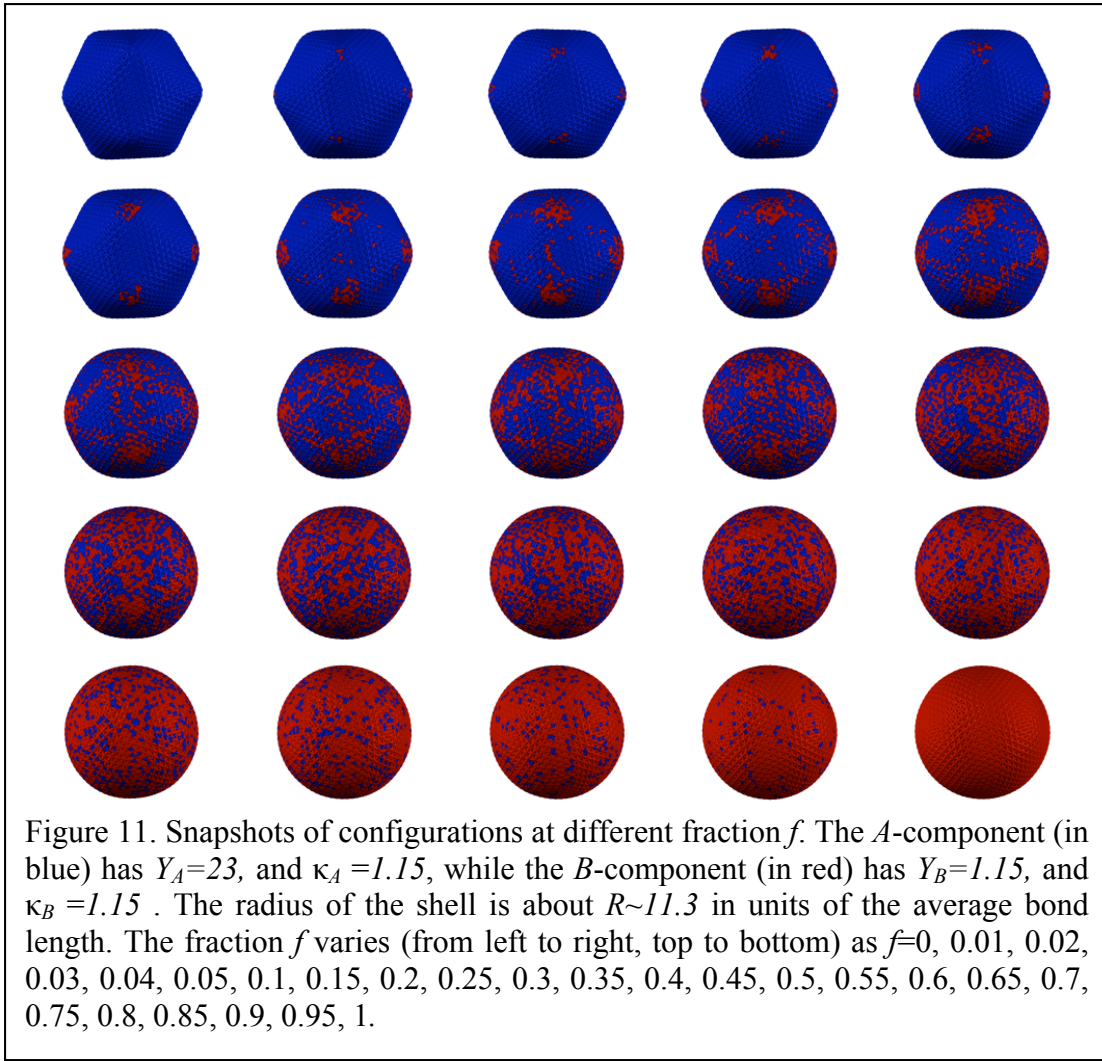
Figure 9: Each elastic component is characterized by two parameters, the bending rigidity κ and the Young's modulus Y, defining a four-dimensional parameter space for a two-component system. Without loss of generality we assume $\kappa_B \geq \kappa_A$. The dotted line indicates the onset of the buckling transition, as determined by the Föppl–von Kármán number γ (see text); above the transition line, the shell at a fixed radius buckles, while below, it stays spherical (flat). *Left panel:* If Y_B is chosen such that a shell rich in B component buckles (blue dot), there are three possible choices for the A component. In regions *I* and *II*, an A-component shell also buckles. In region *III* the A-component shell stays flat, resulting in competition between two components, one of which tends to buckle (B) and the other that prefers to stay flat (A). Simulations for a single disclination disks (Figure 7) were performed in this region, as indicated by the green dot. *Right panel:* For Y_B chosen in the region where the B-component shell is spherical (flat) there are four ways to choose parameters for component A. Regions *V* and *VII* are of little interest because the A-component shell also prefers spherical (flat) geometry. Shape competition occurs in regions *IV* and *VI*, where a shell entirely made of component A buckles. The red dots indicate the parameters for which the Monte Carlo simulations were performed (see Figure 1 in the article and Figures 10 and 11 below). The shaded area indicates the redundant region where $\kappa_A > \kappa_B$.

2. Gallery of shapes

In Figures 10 and 11 we show snapshots of relaxed shapes obtained from Monte Carlo simulations for a range of fractions f of the hard component. In Figure 10 we set $Y_A=Y_B$, in order to drive the faceting via the difference in the bending rigidity between the two components. This is reinforced by the results obtained for $\kappa_A=\kappa_B$ (Figure 11), but with a different Young's modulus, where a smooth transition between sphere and icosahedron is found. In terms of the parameter-space diagram in Figure 9, the strongest faceting effect occurs between regions IV and VI. This is to be expected, as faceting requires the curvature to concentrate in the region along edges between two faces, which is energetically favorable only if a component with small κ is present. Therefore, faceting will be favored for shells with two components having comparable Young's modulus, but sizably different bending rigidity.

Notable examples of regular and irregular polyhedra are bacterial microcomponents, which are shells constructed from proteins involved in a large number of metabolic processes (3). They are D=100-150nm in diameter with the outer shell built entirely of proteins. The shell is d=3-4nm thick and very heterogeneous, typically consisting of up to 20,000 proteins of 10-20 different types. Their relatively large size and small thickness, d/D<<1, renders the elastic theory for thin shells applicable to these microcomponents. Elastic theory of thin shells(1) predicts that $Y\sim d$, while $\kappa\sim d^3$, and we have for simplicity assumed that the three-dimensional Poisson ratio for both components is equal.

Therefore, even a small variation in thickness, caused by different sizes of shell proteins for example, will result in a much stronger change in κ than in Y. This is consistent with our observation that the faceting is much more sensitive to variations in the bending rigidity than in the Young's modulus, and might explain the faceted to non-icosahedral shapes of cellular microcomponents.


Figure 10. Snapshots of configurations at different fraction f. The A-component (in blue) has Y_A= 11.5, and κ_A =0.6, while the B-component (in red) has Y_B=11.5, and κ_B =11.5 . The radius of the shell is about $R\sim11.3$ in units of the average bond length. The fraction f varies (from left to right, top to bottom) as f=0, 0.02, 0.04, 0.1, 0.15, 0.2, 0.3, 0.35, 0.4, 0.5, 0.55, 0.65, 0.7, 0.75, 0.8, 0.85, 0.9, 0.95, 0.955, 0.96, 0.965, 0.975, 0.977, 0.985, 1.

Figure 11. Snapshots of configurations at different fraction *f*. The *A*-component (in blue) has $Y_A=23$, and $\kappa_A =1.15$, while the *B*-component (in red) has $Y_B=1.15$, and $\kappa_B =1.15$. The radius of the shell is about $R\sim11.3$ in units of the average bond length. The fraction *f* varies (from left to right, top to bottom) as *f*=0, 0.01, 0.02, 0.03, 0.04, 0.05, 0.1, 0.15, 0.2, 0.25, 0.3, 0.35, 0.4, 0.45, 0.5, 0.55, 0.6, 0.65, 0.7, 0.75, 0.8, 0.85, 0.9, 0.95, 1.

3. Analysis of FvK number

In order to illuminate the difference between two possible discretizations, the first assigning the elastic properties to the edges, and the second being the more common vertex-based definition, we compare the onset of a buckling transition of a homogeneous sphere with Young modulus and bending rigidity defined on edges or vertices. We scan a range of FvK numbers γ, and compute the asphericity, $\frac{1}{N}\sum_{i=1}^{N}\frac{\left(R_i-\langle R\rangle\right)^2}{\langle R\rangle^2}$, where R_i is the distance of vertex *i* from the center, and <R> is the average radius. For a sphere, the

asphericity is zero, and it increases as the object gradually deforms away from a spherical shape. In Figure 12 we show asphericity as a function of FvK number for a (p,q)=(6,6) sphere with the Young modulus Y and the bending rigidity κ defined on vertices (red) or edges (green). We note that that both definitions result in the same curve.

Figure 12: Asphericity as a function of the FvK number for Young modulus Y and bending rigidity κ defined on vertices (red) or edges (green).
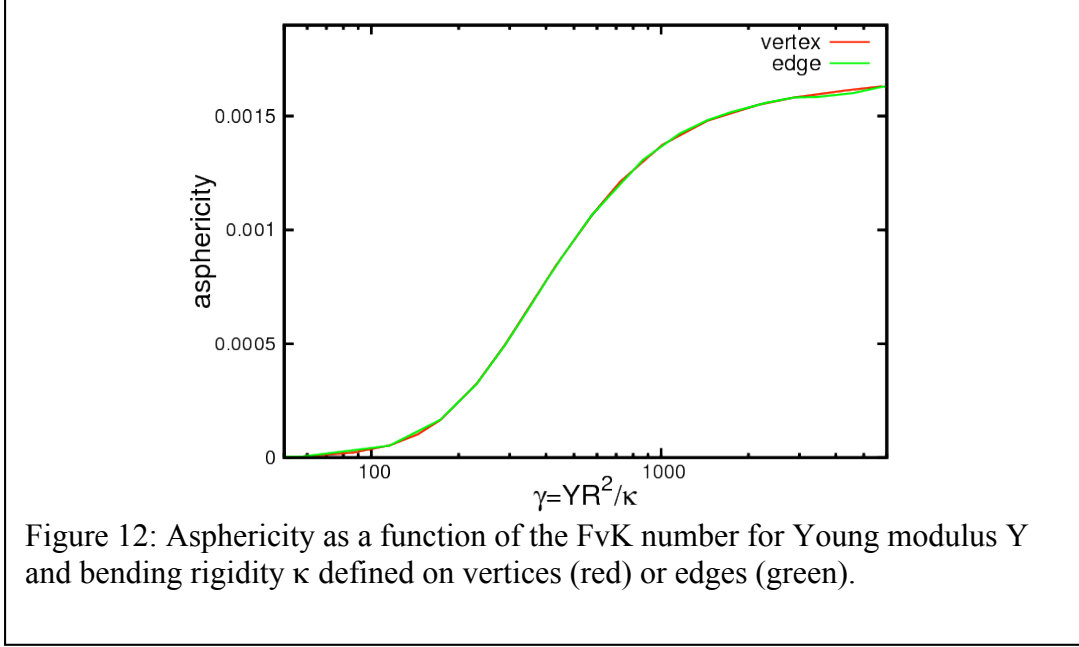
4. Effects of line tension

We briefly address the effects of line tension on faceting as discussed in this study. Here we use a simplest definition of the line tension, where the contact between two vertices of different type is penalized by λ, i.e., $\frac{\lambda}{2}\sum_{\langle i,j \rangle}\left(1-\delta_{t_i,t_j}\right)$, with $\delta_{ti,tj}$ being the Kronecker delta symbol equal to one if both vertices i and j are of the same type. Note that this definition requires the components being placed on vertices rather than on edges,

which does not pose a problem as shown above. We also point out that in our definition of the line tension, λ has units of energy.
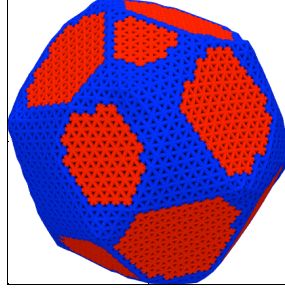
In Figure 13 we show snapshots of the relaxed shapes of a $(p,q)=(12,3)$ elastic shell with 50% of the soft component for a number of values of the line tension. For small λ one observes faceting essentially identical to the case with no line tension. As the line tension is increased, the components segregate and form patches. At intermediate values of λ, we find plate-like regions of the hard component separated by the soft material. At very large values of λ, the components fully phase-separate, and we observe Janus-like structures, where the shape of each section is determined by its local elastic properties, accounting for the hemisphere of the hard component and the buckled region on the soft side. A full study of the properties of multicomponent elastic shells in the presence of line tension between components will be published elsewhere.
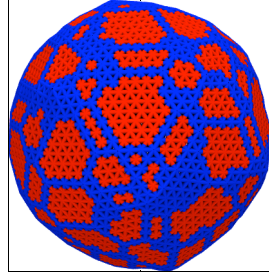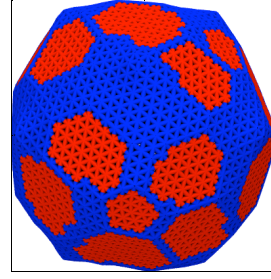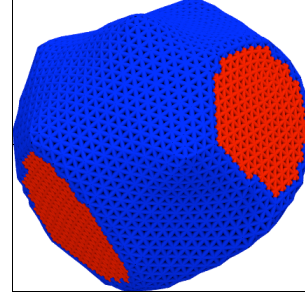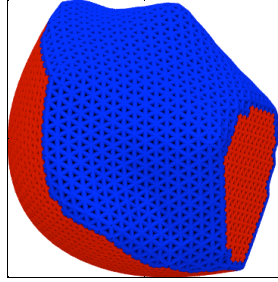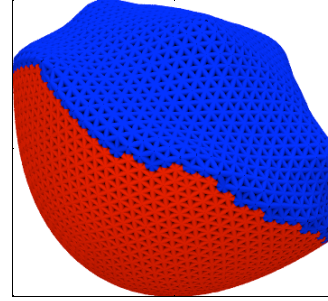
Figure 13: Snapshots of the relaxed shapes of a (p,q)=(12,3) elastic shell with 50% of soft component (blue) with line tension λ=0(a), 0.1(b), 0.3(c), 0.5(d), 0.6(e), 1.0(f). Y_A= 5.77, κ_A =0.06, while Y_B=5.77, and κ_B =28.9. Note that in our model the line tension λ has units of energy.

References and notes

1. Landau LD & Lifshits EM (1970) *Theory of elasticity* (Pergamon Press, Oxford, New York,) 2d English Ed pp viii, 165 p.

2. Seung HS & Nelson DR (1988) Defects in Flexible Membranes with Crystalline Order. *Physical Review A* 38(2):1005-1018.

3. Cheng SQ, Liu Y, Crowley CS, Yeates TO, & Bobik TA (2008) Bacterial microcompartments: their properties and paradoxes. *Bioessays* 30(11-12):1084-1095.